Bayona, V. & Kindelan, M. (2013). Propagation of premixed laminar flames in 3D narrow open ducts using RBF-generated finite differences. *Combustion Theory and Modelling,* 17(5), 789-803.

DOI: 10.1080/13647830.2013.801519

Propagation of premixed laminar flames in 3D narrow open ducts using RBF-generated finite differences

Victor Bayona, Manuel Kindelan
Gregorio Millán Institute,
Universidad Carlos III de Madrid,
28911 Leganés, Spain

March 22, 2013

Abstract

Laminar flame propagation is an important problem in combustion modeling for which great advances have been achieved both in its theoretical understanding and in the numerical solution of the governing equations in two and three dimensions. Most of these numerical simulations use finite difference techniques on simple geometries (channels, ducts, ...) with equispaced nodes. The objective of this work is to explore the applicability of the RBF-generated finite differences (RBF-FD) method to laminar flame propagation modeling. This method is specially well suited for the solution of problems with complex geometries and irregular boundaries. Another important advantage is that the method is independent of the dimension of the problem and, therefore, it is very easy to apply in 3D problems with complex geometries. In this work we use the RBF-FD method to compute two- and three-dimensional numerical results that simulate premixed laminar flames with different Lewis numbers propagating in open ducts.

1 Introduction

Premixed flame propagation is an important topic in combustion research with many applications in engineering and industry safety. It arises in all occasions that a mixture of fuel and air occurs, and therefore the mixture can be ignited leading to a propagating flame. Thus, it is important to understand this physical process which very often takes place in complex shaped domains. One important tool to achieve this goal is the numerical simulation of the equations describing flame propagation. In the past, finite differences (FD) [1–5] and finite element methods (FEM) [6, 7] have been successfully used.

In recent years, radial basis function (RBF) methods has been widely investigated. The main feature of RBF methods is its mesh-independence, relying not on the location but on the distance between RBF centers. This fact makes RBF methods basically

the same for any dimension and for any shape of the domain. Furthermore, they are conceptually simple and easy to implement. There are two different formulations of the RBF method: the global RBF method [8–12] and the local RBF method [13–17] also known as *RBF-generated finite differences* (RBF-FD). In the global RBF formulation, full differentiation matrices are constructed based on RBF interpolants. This formulation is spectrally convergent independently of the distribution of RBF centers. Its principal drawback is that, as the overall number of centers increases, the condition number of the differentiation matrix increases, and this fact restricts the applicability of the method to large scale problems where a great number of RBF centers is needed. In the RBF-FD formulation, the spectral convergence is lost. However, the method has the great advantage that the resulting differentiation matrices are sparse and well-conditioned even for large scale problems in complexly shaped domains [13, 18–20].

In this work we have used RBF-FD to numerically solve a three-dimensional model for the propagation of flames in open circular ducts. Since our focus is to explore the feasibility of the RBF-FD method for the solution of flame propagation problems, we use a simple Arrhenius reaction term to model the chemistry.. However, complex chemistry models can be easily incorporated since the RBF-FD method applies only to the modeling of the space derivative terms. We use stencils with a relatively large number of nodes and, in this way, we are able to achieve high order approximation accuracy. This approach was first used by [18, 19, 21], which were the first to propose the use of RBF-FD with large local stencils in order to achieve both high accuracy and well-conditioning.

The article is organized as follows: Section 2 describes the mathematical model; Section 3 introduces the RBF-FD formulation and explains the numerical implementation of the model; Section 5 presents the two- and three-dimensional numerical results and Section 6 summarizes the conclusions of the present work.

2 Mathematical model

The mathematical model which describes the propagation of laminar flames in open ducts of circular cross-section [5], written in the reference frame moving with a speed $V(t)$ relative to the solid wall, takes the form

$$\frac{\partial T}{\partial t} + V(t)\frac{\partial T}{\partial z} = \Delta T + \omega\left(T, Y\right), \tag{1a}$$

$$\frac{\partial Y}{\partial t} + V(t)\frac{\partial Y}{\partial z} = \frac{1}{Le}\Delta Y - \omega\left(T, Y\right), \tag{1b}$$

where Δ is the laplacian, Y denotes the mass fraction of reactant, T the non-dimensional temperature, z the longitudinal coordinate along the duct and $\omega\left(T, Y\right)$ the non-dimensional reaction rate, which is assumed to follow an Arrhenius law of the form

$$\omega\left(T, Y\right) = \frac{Ze^{\,2}}{2\,Le\;\;{u_p}^2} Y \exp\left[\frac{Ze\left(T-1\right)}{1+\gamma\left(T-1\right)}\right]. \tag{2}$$

The non-dimensional parameters Le, Ze and γ are the Lewis number, the Zeldovich number and the heat release ratio, respectively. u_p is the non-dimensional quantity

$$u_p = S_L/U_L = 1 - \frac{3\gamma + Le - 2.344}{Ze},$$

based on laminar burning velocity of planar flame [22]. In the following simulations, $Ze = 15$ and $\gamma = 0.8$ for different values of the Lewis number Le and the duct radius R. Two different cases are considered: an adiabatic wall,

$$\left.\frac{\partial Y}{\partial r}\right|_{r=R} = 0, \qquad \left.\frac{\partial T}{\partial r}\right|_{r=R} = 0,$$

and an isothermal wall,

$$\left.\frac{\partial Y}{\partial r}\right|_{r=R} = 0, \qquad T|_{r=R} = 0.$$

In both cases,

$$\begin{aligned} Y &= 1, & T &= 0; & x &\to -\infty, \\ \frac{\partial Y}{\partial z} &= 0, & \frac{\partial T}{\partial z} &= 0; & x &\to +\infty, \end{aligned}$$

far upstream and downstream of the flame front, respectively. The temperature T and concentration Y are assumed to be 2π-periodic functions of the azimuthal coordinate ϕ.

As initial conditions we have used

$$Y(z) = \frac{1}{1 + e^{25(z - z_0)}} \qquad \text{and} \qquad T(r, \phi, z) = [1 - Y(z)]\, f(r, \phi) \tag{3}$$

in the adiabatic case and

$$Y(z) = \frac{1}{1 + e^{25(z - z_0)}} \qquad \text{and} \qquad T(r, \phi, z) = \left[\frac{1 - Y(z)}{1 + e^{25(r - 0.8R)}}\right] f(r, \phi) \tag{4}$$

in the isothermal case, where z_0 is the initial location of the flame and $f(r, \phi)$ is a function which modules the amplitude of the initial condition.

3 RBF-FD formulation

RBF-FD can be considered as a natural generalization of classical finite differences [13, 19, 23]. Given a PDE and a set of RBF centers $\{\mathbf{x}_j\}_{j=1}^N$, the spatial differential operator $\mathcal{L}[\cdot]$ is approximated at $\mathbf{x}_i$ by a linear combination of the values of the unknown function $u(\mathbf{x})$ at the $n-1$ closest scattered nodes surrounding $\mathbf{x}_i$,

$$\mathcal{L}[u(\mathbf{x}_i)] \approx \sum_{j \in \sigma_i} \alpha_{ij} u(\mathbf{x}_j), \tag{5}$$

where α_{ij} are the weighting coefficients and $\sigma_i = \{\sigma_i(j)\}_{j=1}^n$ is a set which contains the indices of the nodes which form the stencil centered at $\mathbf{x}_i$. To determine the unknown coefficients α_{ij}, function $u(\mathbf{x})$ is interpolated in (5) by a local RBF interpolant of the form

$$\mathcal{I}_n u(\mathbf{x}) = \sum_{k \in \sigma_i} \lambda_k \, \phi(||\mathbf{x} - \mathbf{x}_k||_2, \, \varepsilon_k),$$

where λ_k is a vector of expansion coefficients and $\phi(||\mathbf{x} - \mathbf{x}_k||_2, \, \varepsilon_k)$ is an RBF. After some algebra, the following linear system of equations results,

$$\mathcal{L}[\phi(||\mathbf{x}_i - \mathbf{x}_k||_2, \, \varepsilon_k)] \; = \; \sum_{j \in \sigma_i} \alpha_{ij} \phi(||\mathbf{x}_j - \mathbf{x}_k||_2, \, \varepsilon_k), \qquad k = \sigma_i(1), \ldots, \sigma_i(n). \tag{6}$$

Its solution yields the weighting coefficients α_{ij}. Notice from equation (6) that RBF-FD is based on enforcing (5) to be exact for RBFs. This procedure guarantees the nonsingularity of (6) even for scattered nodes [24, 25]. The principal consequence is that, independently of the node distribution, the dimension or the shape of the domain, the RBF-FD weighting coefficients are obtained by just solving (6). FD uses instead multivariate polynomials which are independent of node location. Thus, this unisolvency property is no longer assured [11, 26]. Notice also that the corresponding RBF-FD weights can be assembled into a differentiation matrix which preserves the inherent sparsity of FD.

In this work, the RBF chosen is the Gaussian (GA),

$$\phi(r, \varepsilon) = e^{-\varepsilon^2 r^2},$$

which belongs to the class of global, infinitely differentiable RBFs containing a free shape parameter ε. For a given stencil size n, the shape parameter affects both the accuracy of the method and the condition number of the system of equations (6). The RBF method is most accurate for smaller values of the shape parameter where the system of equations is ill-conditioned. This can be clearly seen in Figure (1), which shows the typical dependence of the error and the condition number on the shape parameter. Notice that the error and the condition number cannot both be kept simultaneously small (this is the so-called *uncertainty principle* [27]). An effective way to select the shape parameter is to specify a value of the shape parameter on each stencil such that the matrix condition number satisfies $\kappa_{min} \leq \kappa \leq \kappa_{max}$ [18, 20]. This strategy yields a value of the shape parameter in the region for which the system of equations (6) is still well-conditioned and the error is close to its minimum value. In this work we take $\kappa_{min} = 10^{12}$ and $\kappa_{max} = 10^{14}$. In general, the values of κ_{min} and κ_{max} must be selected for each problem [18, 20]. However, if the number of nodes in the stencil is high enough, the minimum error is obtained just before ill-conditioning and, therefore, values of the condition number κ close to 10^{14} usually work fine.

Notice that if the system of equations is well-conditioned for small values of the shape parameter, then a much lower error would be obtained [10]. To avoid ill conditioning, high precision arithmetic can be used [28]. However, the corresponding computational

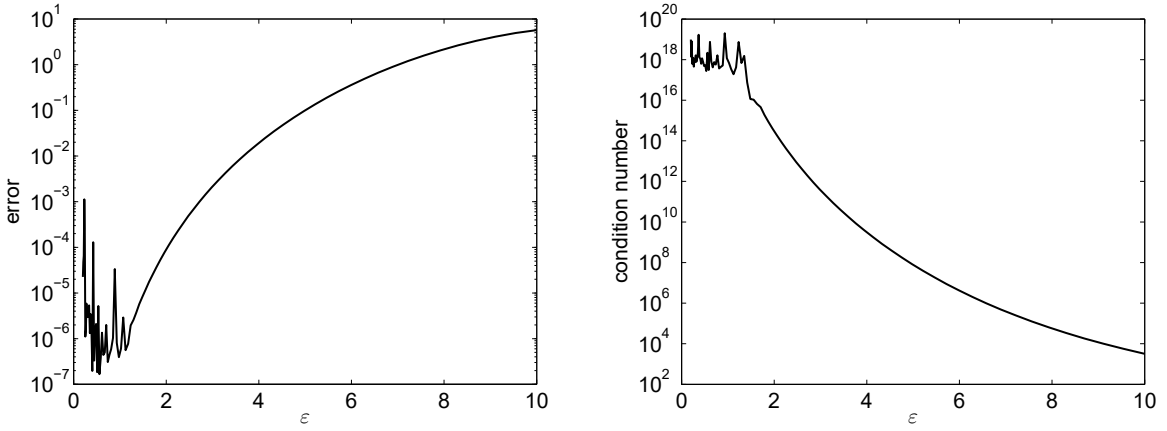

Figure 1: Dependence of the error (left) and the condition number (right) on the shape parameter ε in the approximation of the laplacian of $u(x, y) = \sin(x)\cos(y)$ at $(0.5, 0.5)$ using a stencil of 41 Halton nodes.

cost would be really high and for practical purposes this approach is not used. Alternatively, stable algorithms that avoid ill-conditioned can be used, and during the last years significant efforts have been devoted to achieve this objective [29–32]. Although the corresponding computational cost of these methods are lower than working with high precision arithmetic, their cost is still high for practical purposes.

4 Numerical implementation

Equations (1a) and (1b) are discretized as

$$\frac{\partial \underline{T}}{\partial t} + V(t)\, D_z \underline{T} = \hat{\Delta}\underline{T} + \underline{\omega}, \tag{7a}$$

$$\frac{\partial \underline{Y}}{\partial t} + V(t)\, D_z \underline{Y} = \hat{\Delta}\underline{Y} - \underline{\omega}, \tag{7b}$$

where D_z and $\hat{\Delta}$ are the RBF-FD differentiation matrices which respectively approximate $\frac{\partial}{\partial z}$ and Δ. $\underline{T}$, $\underline{Y}$ and $\underline{\omega}$ represent functions T, Y and ω evaluated at centers $\{\mathbf{x}_j\}_{j=1}^N$.

In order to prevent the flame from leaving the computational domain as time evolves, we follow the method described in [4,5]. In these works, the authors attach the frame of reference to some point $\mathbf{x}^* = (r^*, \phi^*, z^*)$ that moves with the forefront of the flame with a speed $V(t_k)$ relative to the solid wall by imposing at this point an arbitrary constant temperature in the range $0.2 < T^* < 0.5$ and $\partial T/\partial z|_{\mathbf{x}^*} \neq 0$. Under these constraints, equation (7a) at the reference point yields

$$V(t_k)\, D_z \underline{T}^* = \hat{\Delta}\underline{T}^* + \underline{\omega}^*.$$

This equation is used at every time step to compute the velocity of the flame $V(t_k)$. After an initial transient period, if the flame propagates with a constant velocity, the

temperature distribution becomes steady in the frame of reference attached to the flame, and the value $V(t_k)$ becomes time independent. This value is the constant flame speed relative to the wall. The criterion for a steady distribution is that

$$\max \frac{\left|\underline{T}^{k+1} - \underline{T}^{k}\right|}{\Delta t} < 10^{-5},$$

where $\underline{T}^{k}$ and $\underline{T}^{k+1}$ are the values of the temperatures at previous and current time levels, respectively. Since the error committed in determining the velocity with this method is $O(\Delta t)$, equations (7a) and (7b) are advanced in time using a first order method in time. It results in the following system of equations

$$\underline{T}^{k+1} = \underline{T}^{k} + \Delta t \left[\hat{\Delta}\underline{T}^{k} + \underline{\omega}^{k} - V(t_k)\, D_z \underline{T}^{k}\right], \tag{8a}$$

$$\underline{Y}^{k+1} = \underline{Y}^{k} + \Delta t \left[\hat{\Delta}\underline{Y}^{k} - \underline{\omega}^{k} - V(t_k)\, D_z \underline{Y}^{k}\right], \tag{8b}$$

where the solution for all interior nodes at time step $k+1$ is computed using the values of the solution at time step k.

Neumann boundary conditions are implemented at every time step in a way similar to that described in [20]. For instance, consider the adiabatic condition

$$\left.\frac{\partial T}{\partial r}\right|_{\mathbf{x}_i} = \left.\left(\frac{\partial T}{\partial x} n_x^i + \frac{\partial T}{\partial y} n_y^i\right)\right|_{\mathbf{x}_i} = 0, \tag{9}$$

where $\mathbf{n}^i = (n_x^i, n_y^i, 0)$ is a normal vector to the surface of the duct at one boundary point $\mathbf{x}_i$. Let α_x and α_y be the stencil weights that respectively discretize the first derivatives with respect to x and y on a stencil formed by one boundary point $\mathbf{x}_i$ and $n-1$ interior nodes and let $\{\sigma_i(j)\}_{j=1}^{n}$ be the set which contains the corresponding node indices. The boundary value $T(\mathbf{x}_i) = \underline{T}_{\sigma_i(1)}$ at time t_{k+1} is given by

$$\underline{T}_{\sigma_i(1)}^{k+1} = -\sum_{j=2}^{n} \frac{\left(n_x^i \alpha_x^j + n_y^i \alpha_y^j\right)}{n_x^i \alpha_x^1 + n_y^i \alpha_y^1} \underline{T}_{\sigma_i(j)}^{k+1},$$

which is calculated from the interior values $\{\underline{T}_{\sigma_i(j)}^{k+1}\}_{j=2}^{n}$ already updated.

5 Numerical Results

In the following sections, we present the results of solving the mathematical model for different values of the Lewis number Le and the duct radius R using a high-order RBF-FD method. We consider both the two-dimensional and the three-dimensional forms of the model, comparing our results with those presented in [5] where the same model has been solved numerically using the classical second-order finite difference formulas.

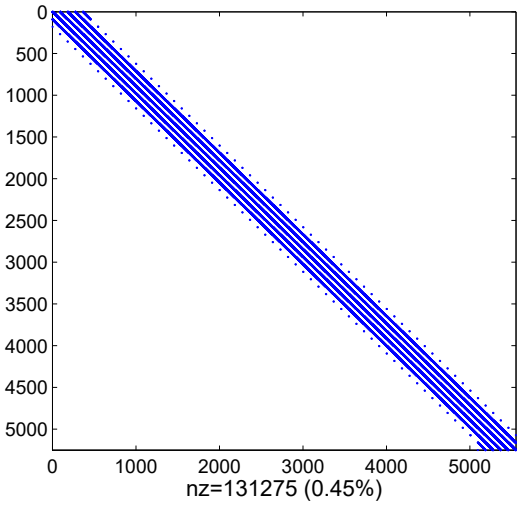

Figure 2: Sparsity of the differentiation matrix $\hat{\Delta}$ using a grid of 91×61 nodes and a 25 node stencil.

5.1 2D-results

In this section we present the results obtained with the two-dimensional form of the model where only coordinates z and r are taken into account and the azimuthal coordinate ϕ is not considered. Hence, the laplacian in equations (1a) and (1b) takes the form $\Delta = \frac{\partial^2}{\partial z^2} + \frac{\partial^2}{\partial r^2} + \frac{1}{r}\frac{\partial}{\partial r}$, where the variables z and r are respectively the longitudinal and radial coordinates and the derivatives with respect to ϕ are zero. Because of the symmetry across the duct centerline, we only consider the region $0 < r < R$ adding the boundary conditions

$$\left.\frac{\partial Y}{\partial r}\right|_{r=0} = 0 \qquad \text{and} \qquad \left.\frac{\partial T}{\partial r}\right|_{r=0} = 0.$$

In our simulations, the upstream and downstream boundaries are placed at $z_{min} = -10$ and $z_{max} = 20$. The resulting domain is discretized using a grid of 91×61 nodes. The stencil size is $n = 25$, which results in an accuracy corresponding roughly with a fourth-order method. The time step size is $\Delta t = 10^{-3}$ except for the case $Le = 0.5$, where we use $\Delta t = 0.5 \cdot 10^{-3}$ to ensure numerical stability. For all stencils, the RBF-FD weights are computed solving (6) with condition numbers in the range $10^{12} \leq \kappa \leq 10^{14}$. In Figure 2 we represent the non-zero elements of the differentiation matrix $\hat{\Delta}$. Notice the high sparsity of RBF-FD for which only 0.45 percent of the elements of the matrix are non-zero.

Figure 3 shows the solution for the case $Le = 1$ and $R = 15$ with isothermal boundary conditions (compare with Figure 2 in [5]). The flame structure has the so-called mushroom-shape. Notice that the flame extinguishes near the wall and the reaction rate increases smoothly towards the axis of the tube, where the flame structure is almost planar. Figures 4 and 5 show solutions corresponding to $R = 20$ and 6, with $Le = 0.7$ and

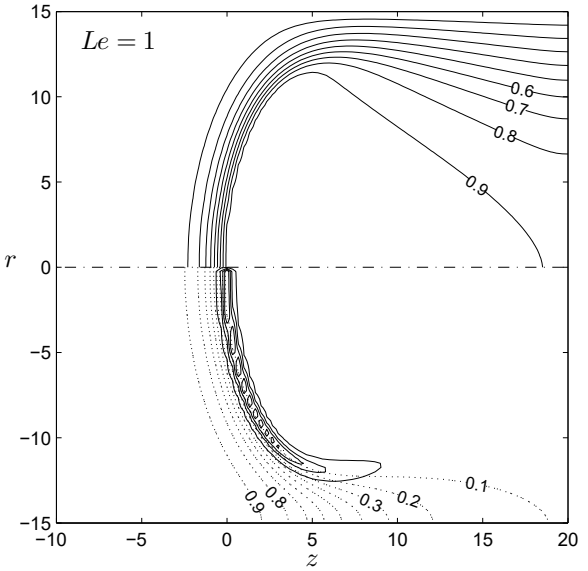

Figure 3: Flame structure for $Le = 1$, $R = 15$ and isothermal wall. Upper half: isotherms (solid lines: T at intervals 0.1, $T_{min} = 0.1$ and $T_{max} = 0.9$). Lower half: fuel mass fraction contours (dotted lines: Y at intervals 0.1, $Y_{min} = 0.1$) and reaction rate contours (solid lines: $\omega = 0.1, 0.5, 1$).

isothermal walls (compare with Figure 3 and 4 in [5]). Notice that for $R = 20$ a two cell solution exists with a structure similar to the tulip flame structure: the forefront of the flame is located near the wall and the flame almost extinguishes near the axis. For $R = 6$, the single cell leading edge is located at the axis of the tube, reaching the maximum temperature just behind the flame front. The corresponding time evolution of the non-dimensional flame velocities and numerical tolerances are plotted in Figure 6. In both cases, the velocity becomes time independent and the tolerance satisfies the criterion for a steady distribution. Similar behavior is observed in all the simulations presented in this work. Figures 7 and 8 (compare with Figure 5 and 6 in [5]) show the adiabatic and isothermal wall solutions for large values of the radius in the case $Le = 0.5$. In both cases it is observed a two cell structure with a similar appearance near the axis of the tube. Nevertheless, the isothermal wall solution produces quenching near the wall and, as a result, the structure of the flame is different in that region.

The problems analyzed in this section are also considered in [5]. It can be appreciated that the RBF-FD solution evolves with the same qualitative features than those presented in the cited work.

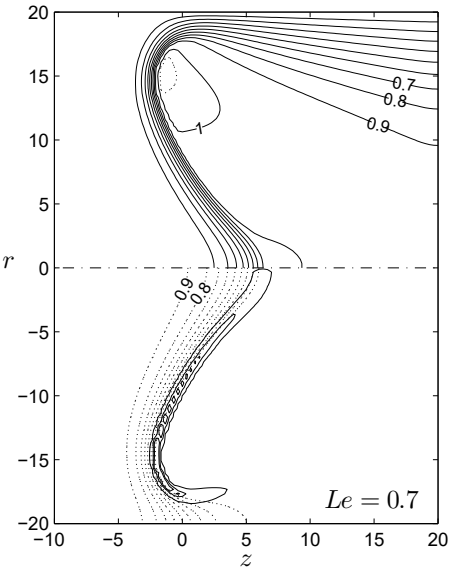

Figure 4: Flame structure for $Le = 0.7$, $R = 20$ and isothermal wall. Upper half: isotherms (solid lines: T at intervals 0.1, $T_{min} = 0.1$ and $T_{max} = 1$; dotted lines: $T = 1.02$). Lower half: fuel mass fraction contours (dotted lines: Y at intervals 0.1, $Y_{min} = 0.1$) and reaction rate contours (solid lines: $\omega = 0.1$, 1, 2).

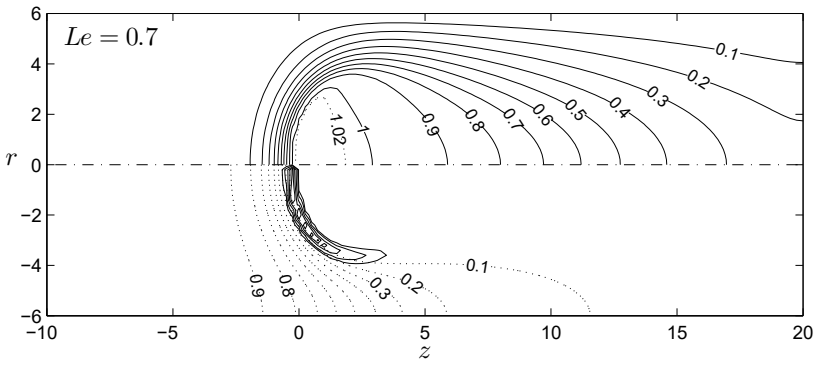

Figure 5: Flame structure for $Le = 0.7$, $R = 6$ and isothermal wall. Upper half: isotherms (solid lines: T at intervals 0.1, $T_{min} = 0.1$ and $T_{max} = 1$; dotted lines: $T = 1.02$). Lower half: fuel mass fraction contours (dotted lines: Y at intervals 0.1, $Y_{min} = 0.1$) and reaction rate contours (solid lines: $\omega = 0.5$, 1, 2, 3, 4).

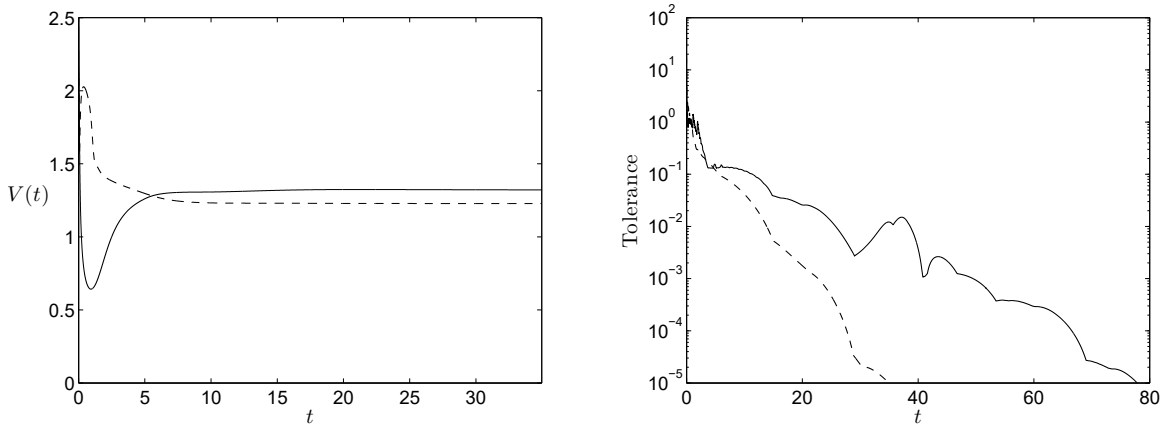

Figure 6: Time evolution of the non-dimensional flame velocity (left) and numerical tolerance (right) for $Le = 0.7$ and $R = 20$ (solid line) and $R = 6$ (dashed line).

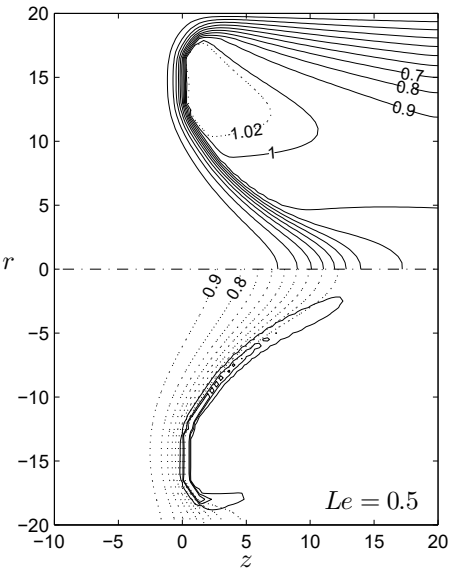

Figure 7: Flame structure for $Le = 0.5$, $R = 20$ and isothermal wall. Upper half: isotherms (solid lines: T at intervals, $T_{min} = 0.1$ and $T_{max} = 1$; dotted lines: $T = 1.02$, 1.04 and 1.06). Lower half: fuel mass fraction contours (dotted lines: Y at intervals 0.1, $Y_{min} = 0.1$) and reaction rate contours (solid lines: $\omega = 0.1$, 1, 2).

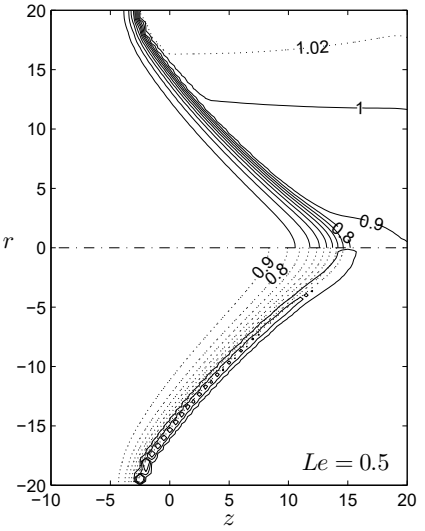

Figure 8: Flame structure for $Le = 0.5$, $R = 20$ and adiabatic wall. Upper half: isotherms (solid lines: T at intervals 0.1 and $T_{min} = 0.1$). Lower half: fuel mass fraction contours (dotted lines: Y at intervals 0.1, $Y_{min} = 0.1$) and reaction rate contours (solid lines: $\omega = 0.1$, 1, 2).

5.2 3D-results

In this subsection we present the results of solving the three-dimensional model in a duct of radius $R = 8$ extending from $z_{min} = -3$ to $z_{max} = 10$, where the upstream and downstream boundaries are respectively placed. This domain is discretized using 6300 nodes as it is shown in Figure 9. The stencil size is $n = 35$, which in three dimensions corresponds roughly with a third-order method. The time step size is $\Delta t = 0.5 \cdot 10^{-3}$ to ensure numerical stability. For all stencils, the RBF-FD weights are computed solving (6) with condition numbers in the range $10^{12} \leq \kappa \leq 10^{14}$. Figure 10 shows the non-zero elements of the differentiation matrix $\hat{\Delta}$ with these settings. As in the two-dimensional case, the matrix is highly sparse with only 0.56 percent of the elements non-zero.

Depending on the initial conditions, the model can reach different steady state solutions for the same set of parameters [5, 33, 34]. For instance, Figures 11 and 12 show the steady state flame structures computed for $Le = 0.5$ and $R = 8$ with isothermal boundary conditions using different initial conditions. Figure 11 shows the isosurface $T = 0.7$ (left) and the longitudinal section of the flame (right). Both reveal an axisymmetric structure similar to that obtained in the corresponding two-dimensional case shown in Figure 7, despite the different radius. Figure 12 shows the isosurface $T = 0.9$ (left) and a longitudinal section of the flame (right). In this case, a complicated flame structure with no axial symmetry is obtained. The right side of the figure reveals that the maximum temperature is reached inside the lobules of the flame. Figures 13 and 14 show respectively the solutions for $Le = 0.5$ and $R = 8$ with adiabatic boundary conditions and $Le = 0.7$

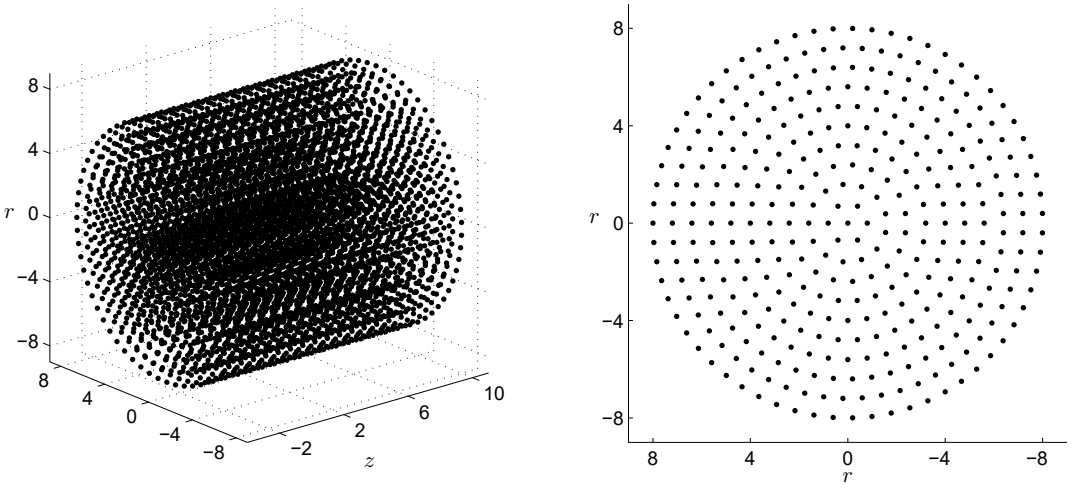

Figure 9: Three-dimensional center distribution with $N = 6300$ (left) and transversal section (right).

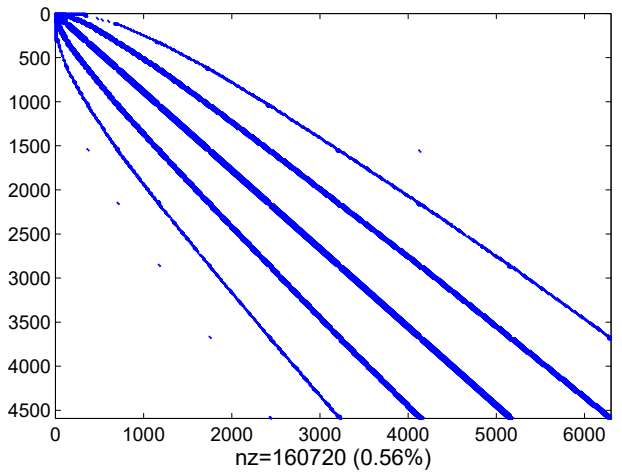

Figure 10: Sparsity of the differentiation matrix $\hat{\Delta}$ using the node distribution shown in Figure 9 and a 35 node stencil.

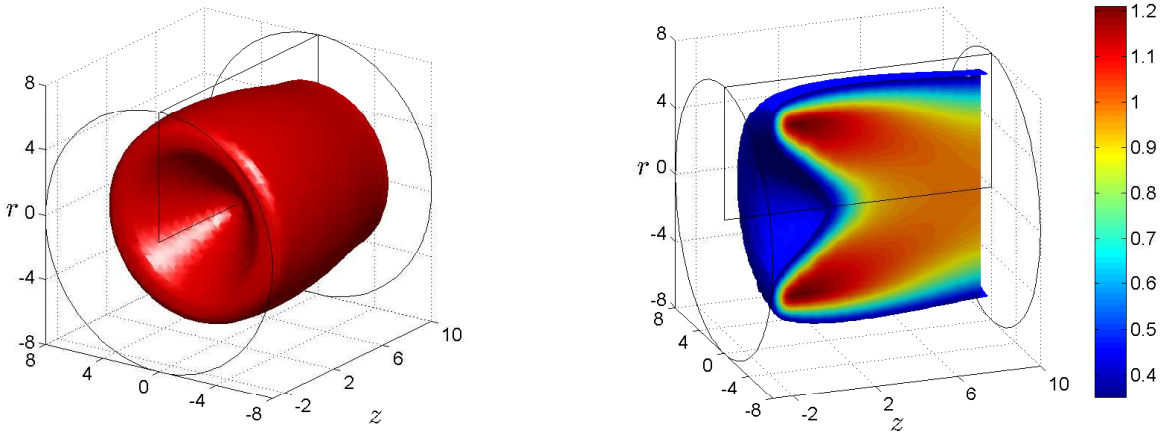

Figure 11: Three-dimensional flame structure for $Le = 0.5$, $R = 8$ and isothermal wall. Left: isosurfaces $T = 0.7$. Right: longitudinal section of the flame.

and $R = 8$ with isothermal boundary conditions. Notice that in both cases the flame structure is not axisymmetric.

Comparing these results with those analyzed in [5], it is observed that the RBF-FD solution evolves with the same qualitative features than those computed with FD. The main advantage of RBF-FD over standard FD is that, as the *Mairhuber-Curtis Theorem* [11,26] points out, in FD it is not possible to compute the weights on arbitrary unstructured stencils in more than 1D, while in RBF methods this problem does not exist [24, 25]. As a result, RBF-FD is able to solve problems using an arbitrary node distribution with high accuracy in space by just increasing the number of nodes in the stencil and/or by choosing appropriately the shape parameter.

6 Conclusions

In this work we analyze the use of RBF-FD to numerically solve a three-dimensional model for the propagation of flames in open circular ducts. The main feature we observe is that RBF-FD is very simple and easy to implement for the solution of a three-dimensional problem. Since its formulation only depends on the distance between centers and not on their location, the method is essentially the same for any dimension and for any shape of the domain. Given an arbitrary node distribution, the RBF-FD method is able to calculate the weighting coefficients that approximate the differential operator by just solving the system of equations (6) for every stencil.

As in FD, the order of the approximation depends on the stencil size. However, RBFs contain a free shape parameter which modifies the accuracy of the approximation [23,35] and the conditioning number of the system of equations. It is more accurate for smaller values of the shape parameter for which the system of equations is ill-conditioned. Hence, accuracy and ill-conditioning cannot be kept simultaneously small. In order to control this

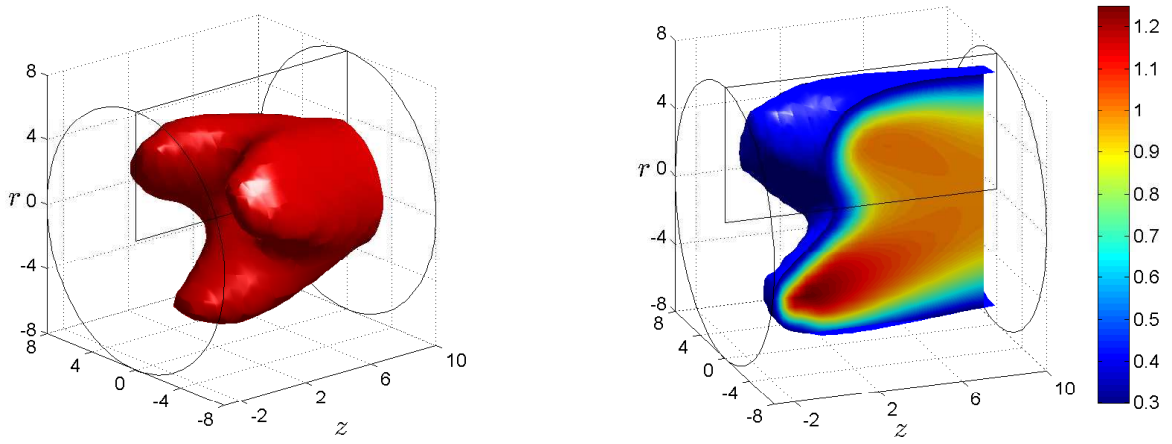

Figure 12: Three-dimensional flame structure for $Le = 0.5$, $R = 8$ and isothermal wall. Left: isosurfaces $T = 0.9$. Right: longitudinal section of the flame.

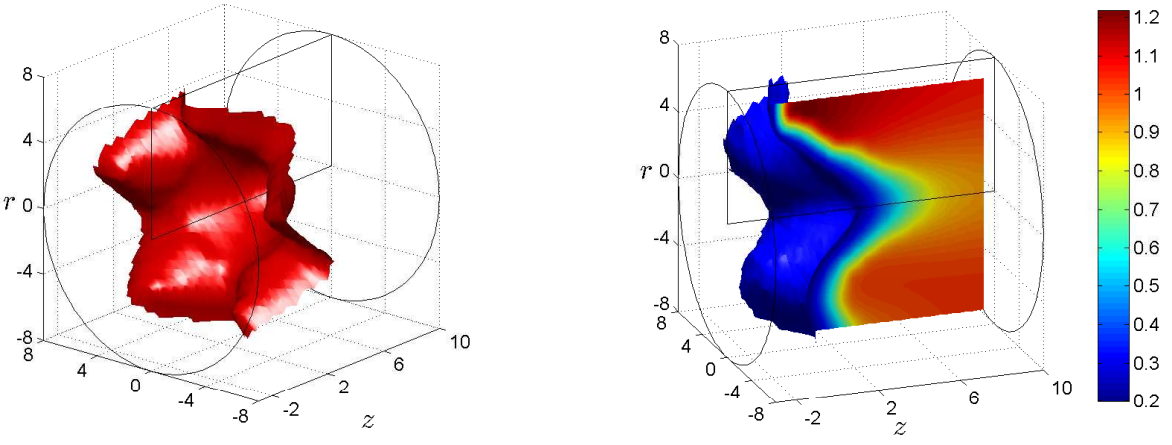

Figure 13: Three-dimensional flame structure for $Le = 0.5$, $R = 8$ and adiabatic wall. Left: isosurfaces $T = 0.8$. Right: longitudinal section of the flame.

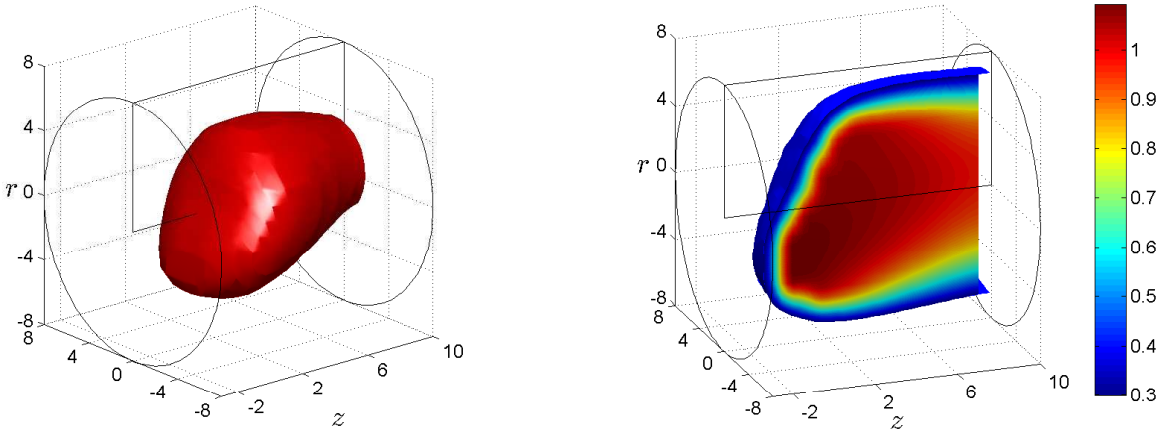

Figure 14: Three-dimensional flame structure for $Le = 0.7$, $R = 8$ and isothermal wall. Left: isosurfaces $T = 0.9$. Right: longitudinal section of the flame.

trade off between accuracy and ill-conditioning, we follow the strategy proposed in [18,20] to select the shape parameter. It is based on specifying a value of the shape parameter on each stencil so that the matrix condition number is bounded, $\kappa_{min} \leq \kappa \leq \kappa_{max}$. This strategy yields a value of the shape parameter which is close to the minimum shape parameter for which the system of equations (6) is still well-conditioned.

Unlike the global RBF method, the resulting differentiation matrices are highly sparse and well-conditioned. In the examples considered, around the 0.5 percent of the elements were non-zero with the corresponding savings in time and memory with respect to the global RBF method. As a result, RBF-FD is a very good alternative to efficiently solve large scales problems in complexly *nth*-dimensional shaped domains [18].

Acknowledgements

This work has been supported by Spanish MICINN grants FIS2010-18473, FIS2011-28838, CSD2010-00011 and by Madrid Autonomous Region grant S2009-1597.

References

[1] G.F. Carrier, F.E. Fendell, and P.S. Feldman. Laminar flame propagation/quench for a parallel-wall duct. *Symposium (International) on Combustion*, 20(1):67–74, 1985.

[2] B. Larrouturou. Adaptive numerical simulation of premixed flame propagation. *Numerical Modeling in Combustion*, pages 133–278, 1993.

[3] N. Peters and J. Warnatz. *Numerical methods in laminar flame propagation*, volume 6. Notes on Numerical Fluid Mechanics. Vieweg & Sohn, 1982.

[4] V.N. Kurdyumov, E. Fernández, and A. Liñán. Flame flashback and propagation of premixed flames near a wall. *Symposium (International) on Combustion*, 28(2):1883–1889, 2000.

[5] V.N. Kurdyumov and E. Fernández-Tarrazo. Lewis number effect on the propagation of premixed laminar flames in narrow open ducts. *Combustion and Flame*, 128(4):382–394, 2002.

[6] J. Fröhlich and J. Lang. Two-dimensional cascadic finite element computations of combustion problems. *Computer Methods in Applied Mechanics and Engineering*, 158(3-4):255–267, 1998.

[7] J. I. Ramos. *Finite element methods for one-dimensional flame propagation problems.* Numerical Modeling in Combustion. T.J. Chung, Taylor & Francis, 1993.

[8] E.J. Kansa. Multiquadrics-a scattered data approximation scheme with applications to computational fluid-dynamics-ii solutions to parabolic, hyperbolic and elliptic partial differential equations. *Computers and Mathematics with Applications*, 19(8-9):147–161, 1990.

[9] E.J. Kansa. Multiquadrics-a scattered data approximation scheme with applications to computational fluid-dynamics-i surface approximations and partial derivative estimates. *Computers and Mathematics with Applications*, 19(8-9):127–145, 1990.

[10] E. Larsson and B. Fornberg. A numerical study of some radial basis function based solution methods for elliptic pdes. *Computers and Mathematics with Applications*, 46(5-6):891–902, 2003.

[11] G.E. Fasshauer and J.G. Zhang. On choosing "optimal" shape parameters for RBF approximation. *Numerical Algorithms*, 45(1-4):345–368, 2007.

[12] Scott A Sarra and Edward J Kansa. Multiquadric radial basis function approximation methods for the numerical solution of partial differential equations. *Tech Science Press*, 1:2, 2010.

[13] G.B. Wright and B. Fornberg. Scattered node compact finite difference-type formulas generated from radial basis functions. *Journal of Computational Physics*, 212(1):99–123, 2006.

[14] A.I. Tolstykh and D.A. Shirobokov. On using radial basis functions in a "finite difference mode" with applications to elasticity problems. *Computational Mechanics*, 33(1):68–79, 2003.

[15] C. Shu, H. Ding, and K.S. Yeo. Local radial basis funcion-based differential quadrature method and its application to solve two-dimensional incompressible navier-stokes equations. *Computer Methods in Applied Mechanics and Engineering*, 192(7-8):941–954, 2003.

[16] YY Shan, C Shu, and ZL Lu. Application of local MQ-DQ method to solve 3D incompressible viscous flows with curved boundary. *Computer modeling in engineering and sciences*, 25(2):99, 2008.

[17] Y.V.S.S. Sanyasiraju and G. Chandhini. Local radial basis function based gridfree scheme for unsteady incompressible viscous flows. *Journal of Computational Physics*, 227(20):8922–8948, 2008.

[18] Natasha Flyer, Erik Lehto, Sébastien Blaise, Grady B Wright, and Amik St-Cyr. A guide to RBF-generated finite differences for nonlinear transport: Shallow water simulations on a sphere. *Journal of Computational Physics*, 231(11):4078–4095, 2012.

[19] B. Fornberg and E. Lehto. Stabilization of RBF-generated finite difference methods for convective pdes. *Journal of Computational Physics*, 230(6):2270–2285, 2011.

[20] Scott A Sarra. A local radial basis function method for advection–diffusion–reaction equations on complexly shaped domains. *Applied Mathematics and Computation*, 218:9853–9865, 2012.

[21] Evan F. Bollig, Natasha Flyer, and Gordon Erlebacher. Solution to PDEs using radial basis function finite-differences (RBF-FD) on multiple GPUs. *J. Comput. Phys.*, 231(21):7133–7151, 2012.

[22] D.G. Lasseigne, T.L. Jackson, and L. Jameson. Stability of freely propagating flames revisited. *Combustion Theory and Modelling*, 3(4):591–611, 1999.

[23] V. Bayona, M. Moscoso, M. Carretero, and M. Kindelan. RBF-FD formulas and convergence properties. *Journal of Computational Physics*, 229(22):8281–8295, 2010.

[24] I. J. Schoenberg. Metric spaces and completely monotone functions. *Annals of Mathematics*, 39(4):pp. 811–841, 1938.

[25] C.A. Micchelli. Interpolation of scattered data: Distance matrices and conditionally positive definite functions. *Constructive Approximation*, 2(1):11–22, 1986.

[26] C. Mairhuber. On haar's theorem concerning chebyshev approximation problems having unique solutions. *Proc. Amer. Math. Soc.*, 7:609–615, 1956.

[27] R. Schaback. Error estimates and condition numbers for radial basis function interpolation. *Adv. Comput. Math.*, 3:251–264, 1995.

[28] C.-S. Huang, C.-F. Lee, and A.H.-D. Cheng. Error estimate, optimal shape factor, and high precision computation of multiquadric collocation method. *Engineering Analysis with Boundary Elements*, 31(7):614–623, 2007.

[29] B. Fornberg and G. Wright. Stable computation of multiquadric interpolants for all values of the shape parameter. *Computers and Mathematics with Applications*, 48(5-6):853–867, 2004.

[30] B. Fornberg and C. Piret. A stable algorithm for flat radial basis functions on a sphere. *SIAM Journal on Scientific Computing*, 30(1):60–80, 2007.

[31] B. Fornberg, E. Larsson, and N. Flyer. Stable computations with gaussian radial basis functions. *SIAM Journal on Scientific Computing*, 33(2):869–892, 2011.

[32] B. Fornberg, E. Lehto, and C. Powell. Stable calculation of gaussian-based rbf-fd stencils. *Computers and Mathematics with Applications*, 65(4):627–637, 2013.

[33] Robert F Heinemann, Knowles A Overholser, and George W Reddien. Multiplicity and stability of premixed laminar flames: An application of bifurcation theory. *Chemical Engineering Science*, 34(6):833–840, 1979.

[34] Serge Galant. Multiplicity and stability of burner stabilized premixed laminar flames: A general proof. In *Symposium (International) on Combustion*, volume 18, pages 1343–1353. Elsevier, 1981.

[35] V. Bayona, M. Moscoso, and M. Kindelan. Gaussian RBF-FD weights and its corresponding local truncation errors. *Engineering Analysis with Boundary Elements*, 36(9):1361–1369, 2012.